

# Experimental investigation into the interference aerodynamics of two slender bodies in close proximity

R. Chaplin · D. MacManus · F. Leopold ·  
T. Gauthier · B. Martinez · T. Birch

Received: 30 January 2010/Revised: 5 July 2010/Accepted: 17 July 2010/Published online: 13 August 2010  
© Springer-Verlag 2010

**Abstract** Aerodynamic interference between high-speed slender bodies can detrimentally affect the force and moment characteristics. This is investigated through a wind tunnel study using pressure sensitive paint and force measurements on a receiver body placed adjacent to a generator body. The aim of this paper is to understand both the force and moment changes as well as the underlying aerodynamics of the interference loads which are induced by the disturbance flowfield. The impact of receiver incidence and the strength of the disturbance field are also assessed. The observed interference loads primarily depend on a complex balance of static pressure footprints and tend to be bespoke to each configuration. As a result, overall trends are difficult to extract, but in general the magnitude of the interference loads increases when the receiver is at incidence and also when the strength of the imposed disturbance flowfield increases.

## List of symbols

$a$  Sonic velocity [ $\text{ms}^{-1}$ ]  
 $A$  Stern–Volmer calibration constant  
 $B$  Stern–Volmer calibration constant

R. Chaplin · D. MacManus (✉)  
Department of Aerospace Sciences, Cranfield University,  
Cranfield, UK  
e-mail: d.g.macmanus@cranfield.ac.uk

F. Leopold · T. Gauthier · B. Martinez  
French-German Research Institute of Saint-Louis (ISL),  
Saint-Louis, France

T. Birch  
Air and Weapon Systems, Defence Science and Technology  
Laboratory (Dstl), Portsmouth West, UK

$C_p$  Pressure coefficient  $C_p = \frac{p-p_\infty}{q_\infty}$   
 $\Delta C_p$  Pressure coefficient difference at given body location  $\Delta C_p = C_p - C_{p,iso}$   
 $C_{X,t}$  Measured axial force coefficient  $C_{X,t} = \frac{F_x}{q_\infty S}$   
 $C_X$  Axial force coefficient corrected to zero base drag  
 $C_Z$  Normal force coefficient  $C_Z = \frac{F_z}{q_\infty S}$   
 $C_m$  Pitching moment coefficient (about  $x = 0$ ,  $y = 0$ ,  $z = 0$ )  $C_m = \frac{M_y}{q_\infty S D}$   
 $\Delta C_Z$  Normal force interference load at a given  $\sigma R$   $\Delta C_Z = C_Z - C_{Z,iso}$   
 $\Delta C_m$  Pitching moment interference load at a given  $\sigma R$   $\Delta C_m = C_m - C_{m,iso}$   
 $D$  Maximum body diameter at base [m]  
 $F_X$  Receiver body axial force (N)  
 $F_Z$  Receiver body normal force (N)  
 $I$  Luminescence intensity for a given pixel  
 $L$  Maximum body length (m)  
 $M_Y$  Receiver body pitching moment (Nm)  
 $M$  Mach number  $M = \frac{U}{a}$   
 $p$  Static pressure ( $\text{Nm}^{-2}$ )  
 $q$  Dynamic pressure ( $\text{Nm}^{-2}$ )  
 $Re_D$  Freestream Reynolds number based upon base diameter  $Re_D = \frac{\rho_\infty U_\infty D}{\mu_\infty}$   
 $Re/m$  Freestream Reynolds number per metre ( $\text{m}^{-1}$ )  
 $S$  Receiver body reference area ( $\text{m}^2$ )  
 $S_b$  Receiver body base area ( $\text{m}^2$ )  
 $T$  Static temperature (K)  
 $U$  Velocity ( $\text{ms}^{-1}$ )  
 $X, Y, Z$  Body fixed axes  
 $X_{cp}$  Longitudinal centre of pressure measured from receiver ( $x = 0$ )  $X_{cp} = C_m/C_Z$  [m]  
 $X_{cg}$  Longitudinal centre of gravity measured from receiver ( $x = 0$ ) [m]  
 $\Delta x$  Axial stagger between bodies (m)

|                  |   |
|------------------|---|
| $x_{\text{res}}$ | Horizontal spatial resolution in the PSP 2D image space (m) |
| $x'$             | Axial impingement location of the primary disturbance (m)   |
| $y_{\text{res}}$ | Vertical spatial resolution in the PSP 2D image space (m)   |
| $\Delta z$       | Lateral separation between bodies (m)                       |

### Greek symbols

|                       |   |
|-----------------------|---|
| $\delta$              | Uncertainty for a given parameter   |
| $\mu$                 | Dynamic viscosity ( $\text{m}^2 \text{s}^{-1}$ )                              |
| $\theta_{s,G}$        | Generator conical bow shock angle, measured freestream flow axis ( $^\circ$ ) |
| $\theta_{\text{obl}}$ | Shock obliqueness angle ( $\theta_{s,G} - \sigma_R$ ) ( $^\circ$ )            |
| $\rho$                | Density [ $\text{kgm}^{-3}$ ]   |
| $\sigma$              | Total incidence angle ( $^\circ$ )  |
| $\sigma_{\text{cor}}$ | Total incidence correction for flow angularity ( $^\circ$ )                   |
| $\sigma_{\text{eff}}$ | Effective total incidence based on interference load ( $^\circ$ )             |
| $\Delta$              | Difference of a given parameter from isolated configuration                   |
| $\phi$                | Receiver azimuth angle ( $^\circ$ )   |

### Subscripts

|          |                                  |
|----------|----------------------------------|
| near     | Receiver nearside conditions     |
| iso      | Isolated conditions              |
| 0        | Stagnation conditions            |
| $\infty$ | (inf) freestream conditions      |
| $R$      | Receiver body                    |
| $G$      | Generator body                   |
| ref      | Wind off PSP reference condition |
| amp      | Ambient conditions               |

## 1 Introduction

Aerodynamic interference occurs when two bodies are placed in close proximity in a high-speed flow and this can significantly affect the force and moment characteristics (Wilcox 1995; Hung 1985). The complex flowfield is primarily dominated by the shock and expansion waves, which originate from an adjacent body (the generator) and impinge upon the primary body of interest (the receiver). The interference aerodynamics is further complicated by multiple shock reflections, shock diffraction as well as shock interactions with the viscous body vortex and boundary-layer flows. The induced changes in static pressure and flow angularity across the impinging disturbances modify both the local and overall aerodynamics of a slender body in comparison with the isolated body case.

Very limited information is available in the open literature on the effects of mutual interference between slender bodies at high speed. One previous investigation showed

that a planar shock impinging on a cone-cylinder body at zero incidence induced changes in normal force and pitching moment coefficient of approximately 0.02 and 0.2, respectively (Wilcox 1995). These changes were found to increase by up to an order of magnitude when the receiver body was placed at an incidence of  $\sigma = 15^\circ$ . Interference effects of this order would modify the trajectory of the slender body and would become significant if the slender body pitches (or translates) towards the generator resulting in a collision. Another study, which investigated two axially aligned slender bodies at zero incidence, found that the polarity of the resulting pitching moment load was strongly dependent upon the lateral separation between the bodies (Volkov and Derunov 2006). This could potentially have a significant effect on the trajectory of both bodies as a result of mutual interference (Malmuth and Shaleav 2004).

In addition to the overall interference loads, it is important to understand the detailed underlying flow physics. Of particular interest are the shock-body interactions which have been studied previously for a number of configurations (Volkov and Derunov 2006; Malmuth and Shaleav 2004; Fedorov et al. 2007; Derunov et al. 2008). Brosh et al. (1985) and Hung (1985) investigated a wedge-generated shock passing over a cylinder at  $M_\infty = 3$ , which showed that the shock footprint, in terms of local pressure rise, decreased as the shock diffracted around the body. In addition, the induced pressure rise on the nearside reduces quickly due to the impact of expansion waves from the generator forebody. These expansion waves do not diffract to the same extent as the impinging shock and thus the farside pressure rise associated with the diffracted shock is maintained along the body. Consequently, the difference between the strength and extent of the nearside and farside interactions significantly affects the local normal force distribution over the body. Finally, the nearside pressure rise also resulted in a local boundary-layer separation and a double-reflected shock structure around the nearside separation bubble. Both studies found that due to the induced circumferential pressure gradient a strong crossflow occurred which resulted in a local separation on the farside of the receiver body. A similar effect was also noted by Morkovin et al. (1952).

The aims of this paper are to quantify the aerodynamic interference loads induced on a slender body and to understand the underlying aerodynamics which cause these loads. To meet these aims, a wind tunnel study has been conducted, where the primary measurements are the receiver forces and moments, surface PSP (Pressure Sensitive Paint) and shadowgraph visualisation. The effects of receiver incidence and disturbance field strength have also been examined. As the PSP technique provides quantitative pressure measurements on a body surface (Lui and Sullivan 2005), it is ideally suited for problems

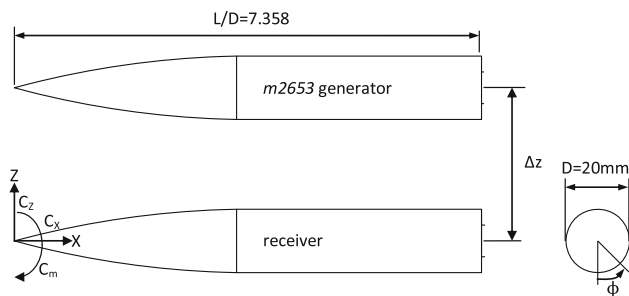


**Fig. 1** Schematic of the multi-body arrangement

where complex pressure footprints are a primary factor in the aerodynamics (Kurita et al. 2001).

## 2 Method

### 2.1 Model descriptions and tunnel set-up

All force and moment and PSP measurements were taken on the receiver body (Fig. 1). This body consists of a  $3.5D$  tangent ogive forebody, a cylindrical afterbody and a total length of  $7.358D$  and a maximum body diameter at the base of  $D = 20$  mm (Fig. 1). Two different generator bodies were used to provide the disturbance flowfield. The sharp generator (designated *m2653*) was identical to the receiver geometry. The blunt generator (designated *m2654*) had the same overall length as the other bodies ( $L/D = 7.358$ ), but included a  $0.5D$  hemi-sphere forebody.

The tests were performed in the  $0.2 \times 0.2$  m blowdown S20 Supersonic Wind Tunnel at the French-German Research Institute of Saint-Louis. The working section operating conditions were  $P_0$  of 0.675 MPa,  $T_0$  of 293 K,  $Re/m$  of  $6.97 \times 10^7$ , and  $M_\infty$  of 2.43. The typical run time was 50 s.

Multi-body testing was performed by using a dual-support system (Fig. 2). A traverse mechanism allowed the upper generator body and lower receiver body to be translated relative to one another in the streamwise direction. The receiver body incidence was controlled using the lower support sting, which rotated about a centre of rotation point  $1.65D$  upstream of the base on the body centreline. Two 16-mm-diameter stings connected each body to their respective supports (Fig. 2).

The generator was maintained at zero incidence ( $\sigma_G = 0^\circ$ ) throughout all tests, while the receiver body incidence ( $\sigma_R$ ) was varied between  $-15 \leq \sigma_R \leq 15^\circ$ . Lateral separation ( $\Delta z$ ) is defined as the distance between the body centrelines at zero incidence (Fig. 1). This was maintained at  $\Delta z/D = 2.94$  in all tests. Axial stagger is defined as the  $x$ -distance between the leading edge of the generator and receiver bodies and is positive when the

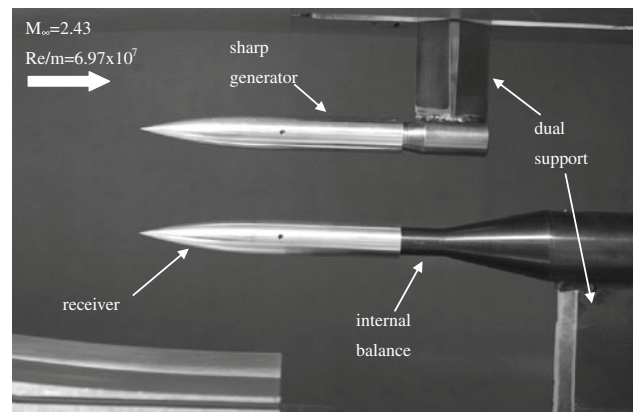


**Fig. 2** Receiver body set-up adjacent to the sharp generator

generator is upstream of the receiver. Due to the different shock structures induced by the different generator forebody shapes, and in order to ensure a constant shock impingement location on the receiver body, axial staggers of  $\Delta x/D = 1.67$  and  $\Delta x/D = -0.53$  were used for the sharp and blunt generator, respectively. The receiver and generator bodies were placed at zero sideslip for all tests. No boundary-layer transition devices were used for the results presented in this paper. However, additional tests of the isolated receiver configuration using a wire transition strip attached 2 mm from the leading edge of the forebody demonstrated a negligible effect on the normal force and pitching moment coefficients and a small increase in axial force of  $\Delta C_{X,t} = 0.01$ . It is therefore assumed that the boundary-layer was naturally turbulent during these tests.

### 2.2 Experiment methodology

The datum configuration comprised the receiver body at zero incidence adjacent to the sharp generator with an axial stagger of  $\Delta x/D = 1.67$ . The effect of receiver incidence was assessed by varying  $\sigma_R$  between  $-15 \leq \sigma_R \leq 15^\circ$ . The receiver body paused at each incidence setting, where the forces were measured using an ABLE MKXIV 6-component, internal balance (Fig. 2). This balance was fitted internally in the lower support and central cavity of the receiver. The force and moment balance output was filtered by a low-pass 5-Hz filter and acquired at a sample rate of 100 kHz with a sample duration of 2 s. The force and moment data were reduced to their non-dimensional coefficient form (Eqs. 1–4). A shadowgraph image was taken at each incidence setting. A light source was focused using a 0.38 m diameter-lens and the illuminated flowfield was projected onto a transparent screen on the opposite tunnel window, where a still image was taken with a PCO Sencam qe camera.

$$C_Z = \frac{F_Z}{q_\infty S} \quad (1)$$

$$C_{X,t} = \frac{F_X}{q_\infty S} \quad (2)$$

$$C_m = \frac{M_Y}{q_\infty S D} \quad (3)$$

$$C_X = C_{X,t} + \frac{S_b(p_b - p_\infty)}{q_\infty S} \quad (4)$$

In this study, a Bi-Luminophore PSP developed by Innovative Scientific Solutions Incorporated (ISSI) was used to obtain surface pressure measurements on the receiver for selected incidence angles. Binary-FIB BF405 contains two luminophore probes, a signal probe (platinum meso-tetra(pentafluorophenyl) porphyrine, Pt(TfPP)) which is sensitive to pressure and a reference probe which is sensitive to illumination but relatively insensitive to pressure. The binder is a FIB (Fluoro/Isopropyl/Butyl) polymer. The luminophore and polymer binder were dissolved in a benzene solvent and a uniform coat was applied by spray-painting the receiver model, which was first cleaned with acetone and polished. The model was cured for 20–30 min at 65°C to evaporate the solvent and immobilise the luminophore probes in the binder. As the Binary-FIB PSP contains TiO<sub>2</sub> particles, there was no need for a screen-layer to mask the natural luminescence of the model or to increase the luminescence reflection of the paint. The Binary-FIB is therefore a uni-coat paint.

$$\frac{I_{\text{ref}}}{I} = A + B \frac{p}{p_{\text{ref}}} \quad (5)$$

The PSP technique relies upon the photo-physical processes involved in luminescence in particular oxygen quenching (Gregory et al. 2008). The underlying principle is expressed in Henry's law (Lui and Sullivan 2005), which states that the concentration of oxygen molecules in the binder is proportional to the partial pressure of the oxygen adjacent to the paint layer. For air, this is proportional to the total air pressure. Consequently, a higher air pressure adjacent to the model surface, results in a reduced intensity of luminescence. The expression that most conveniently describes the relationship between air pressure and luminescence intensity is the Stern–Volmer relation (Lui and Sullivan 2005). The constants  $A$  and  $B$  are experimentally determined calibration coefficients,  $I_{\text{ref}}$  and  $I$  are the intensities for a known and unknown pressure condition, respectively. Similarly,  $p_{\text{ref}}$  and  $p$  are the pressures associated with a known and unknown test condition, respectively (Eq. 5).

For a given configuration, the painted receiver model was placed on the lower support (Fig. 2) and approximately 10 reference points were marked on the surface to

aid with the post-test image re-alignment. Two ISSI UV LM2X-405 LED lamp modules were placed on an optics bench immediately adjacent to the working section. These were positioned approximately  $\pm 45^\circ$  to the camera line-of-sight, which was set-up normal to the tunnel axis in the lateral direction. These provided illumination light at a wavelength of 405 nm. The emitted luminescence was measured with a 12-bit PCO Sencicam qe camera, a Cosmicar TV manual zoom lens (12.5–75 mm 1:1.8) and an Andover FS20-50 bandwidth optical filter with a pass wavelength of 650 nm.

'Wind-off' images were acquired at each incidence ( $\sigma_R = 0, \pm 8^\circ, \pm 15^\circ$ ) which provided the reference intensity ( $I_{\text{ref}}$ ) values for each pixel, where the reference atmospheric conditions were known ( $p_{\text{ref}} = p_{\text{amb}} = 1$  atm and  $T_{\text{amb}} = 20^\circ\text{C}$ ). Under 'wind-on' conditions the receiver was pitched through each of the incidence settings with a 5 s pause at each. This was sufficient for time-independent pressure measurements as the Binary-FIB paint has a time response of 0.3 s (Pulkin et al. 2000). A wind-on image was acquired which measured the light intensity ( $I$ ) and is related to the associated unknown pressure ( $p$ ) for each pixel. At the end of each run, the models were removed and replaced by a 3D check-board with  $10 \times 10 \times 10$  mm squares. The acquired image of this calibration model was used to transform the 2D image space into a known 3D co-ordinate system and was large enough to cover the complete movement of the receiver body. Finally, a 'black image' was also taken with the lens covered to identify the baseline noise level in the camera measurement system.

An intensity-based PSP method was used to calculate the unknown pressures on the receiver body. In general, a ratio of the wind-off and wind-on images is used to mitigate the effects of uneven PSP coating, non-homogeneous luminophore concentration in the PSP layer and non-uniform illumination (Lui and Sullivan 2005). The use of LED lamps further ensured that there was a negligible change in the illumination intensity between the wind-off and wind-on images. Due to aeroelastic deformation of the receiver body under aerodynamic loading and wind tunnel vibrations, the wind-on image was offset from the wind-off image. Therefore, the wind-on image was re-aligned to fit precisely over the wind-off image using the reference marker points. The black image intensity (typically in the order of 0.5% of the total intensity levels) for each pixel was subtracted from both images and then a pixel-on-pixel intensity ratio was calculated ( $I_{\text{ref}}/I$ ). For a given intensity ratio ( $I_{\text{ref}}/I$ ), the associated pressure ( $p$ ) was found from the Stern–Volmer calibration curve (Lui and Sullivan 2005) and knowledge of  $p_{\text{ref}}$  (Eq. 5). The pressure data in the 2D image space was mapped onto a 3D surface mesh of the receiver body, which contained

**Table 1** Summary of experimental uncertainties

| Tunnel arrangement  | Freestream conditions                 | Force measurements (%)   | PSP measurements                       |
|---------------------|---------------------------------------|--|--|
| $\Delta x/D$        | $1.67 \pm 1.5\%$<br>$-0.53 \pm 4.7\%$ | $M_\infty$ $2.43 \pm 0.2\%$<br>$Re/m$ $6.97 \times 10^7 \pm 0.7\%$ | $C_{x,t}$ $\pm 0.6$<br>$C_x$ $\pm 2.5$ |
| $\Delta z/D$        | $2.94 \pm 0.1\%$                      | $C_z$ $\pm 0.6$  | $p$ $\pm 5\%$                          |
| $\delta_{\sigma R}$ | $\pm 0.1^\circ$                       | $C_m$ $\pm 0.6$  |  |
| $\delta_{\sigma G}$ | $\pm 0.1^\circ$                       |  |  |
| $\delta_{\sigma/L}$ | $\pm 0.01$                            |  |  |

approximately 200,000 nodes. The spatial resolution in the 2D image space was estimated to be  $x_{\text{res}} = y_{\text{res}} = 0.13$  mm, based on the number of camera pixels ( $1,376 \times 1,040$ ). Since only one camera was used, its spatial position with respect to the model was used to determine whether a given node was in view or not. All hidden nodes were assigned zero pressure.

At the extremes of surface curvature (especially near the receiver leading edge,  $x/L \leq 0.15$ ), the local surface normal was almost perpendicular to the camera line-of-sight and the data in this small region were considered to be unreliable and excluded from the pressure plots. As a result, pressure data are extracted at  $\phi = 177^\circ$  and  $\phi = 3^\circ$  on the receiver nearside and farside, respectively. Although the camera viewing angle is low at these locations, analysis of the “wind-off” images showed that the signal strength was sufficient to obtain data within the estimated uncertainty levels. Due to wind tunnel debris a small amount of degradation of the PSP coating occurred during each test. In addition, the model attachment screw hole caused a local flowfield disturbance at  $x/L \approx 0.55$  and  $\phi = 90^\circ$ . The latter two aspects did not have a significant impact on the interaction footprints and thus are neglected in the interference analysis.

### 2.3 PSP calibration

The Stern–Volmer calibration curve was determined from an a-priori calibration of a sample of Binary-FIB tested over a controlled pressure and temperature range. In this study, the calibration chamber tested a paint sample on a  $40 \times 40$  mm copper plate for which the local temperature was regulated using a two-stage Peltier cell. The sample temperature was measured with a thermistor, which was placed in a hollow moulding under the paint sample. The chamber pressure was regulated and measured using a piezoresistive sensor. The reference intensity ( $I_{\text{ref}}$ ) was first measured under ambient conditions of  $p_{\text{amb}} = p_{\text{ref}} = 1$  bar and  $T_{\text{amb}} = 293.2$  K. At constant temperature, different pressure levels were applied over a range of  $2 \text{ mbar} \leq p \leq 5$  bar and the intensity recorded using the same acquisition system as previously described. This was repeated for different temperature

settings. A 5th order polynomial was fitted to the Stern–Volmer relation (Eq. 5). Due to the ideality of the Binary-FIB paint (Pulkin et al. 2000), the resulting Stern–Volmer curves were relatively insensitive to temperature (0.03%/K) but showed a large sensitivity to pressure (4.5%/psi). This is because the reference luminophore compensates for changes in temperature between the reference and measurement conditions. Consequently, it was not necessary to measure the model surface temperature for correction of the PSP data.

### 2.4 Experimental uncertainty

The experimental uncertainties were calculated using the approach of Taylor (1997) and mostly expressed as a fractional uncertainty of the measured value (Table 1). All measurement uncertainties were estimated from bias and statistical sources of error which included the instrument calibration, instrument accuracy given by the manufacturer and the data acquisition resolution. The measured free-stream conditions and force and moment measurements were found to be highly repeatable over consecutive wind tunnel runs (Chaplin 2009). As an example, the worst case variation between measurements of the isolated receiver over four consecutive runs was in the order  $C_{x,t} = 0.01$ ,  $C_z = 0.03$  and  $C_m = 0.2$ . The uncertainty in the PSP measurement is based on the difference between the PSP and an in situ static pressure measurement taken on the balance near the model base. As with the force and moment measurements, the PSP measurements were also repeatable over two consecutive runs.

## 3 Results and discussion

The aim of this study is primarily to understand the underlying aerodynamic characteristics and mechanisms associated with the imposed disturbance field for the receiver slender body. However, the interference aerodynamics and the different flow features are very sensitive to the individual configuration and consequently generic trends and features are difficult to extract. As the focus is on understanding the detailed aerodynamics, the results are

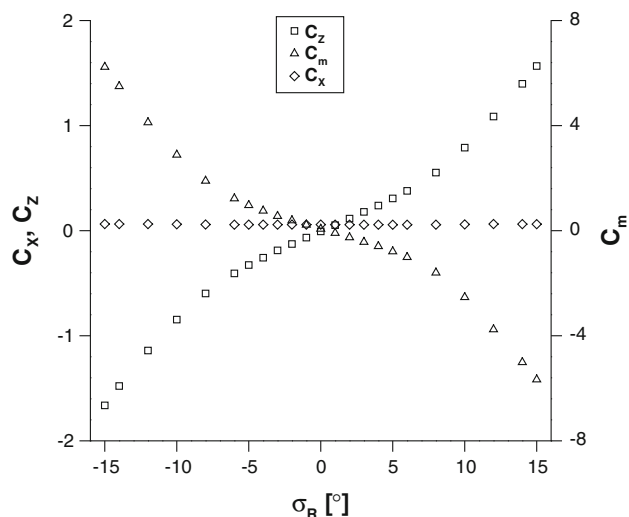


**Fig. 3** Force and moment coefficient distributions as a function of incidence for an isolated receiver body

presented in a way which separately considers the effects of the main configuration parameters. In each of these sections, due to the distinctive underlying flow physics, the flowfield is investigated in detail to explain the reasons behind the observed interference loads and to highlight particular aerodynamic mechanisms that come to the fore. Before investigating the multi-body configurations, the force and moment characteristics of the isolated receiver are briefly discussed to introduce the reference aerodynamics for the receiver body.

### 3.1 Isolated aerodynamics

Due to a small asymmetry in the working section, a flow incidence correction of  $\sigma_{\text{cor}} = -0.1^\circ$  is applied to the experimental force and moment data for the isolated receiver configuration. This ensures zero normal force at zero incidence. The measured force and moment characteristics of the receiver body are typical of a high-speed, slender body with a non-linear variation in normal force ( $C_z$ ) and pitching moment ( $C_m$ ) with incidence ( $\sigma_R$ ), Fig. 3. As expected, the axial force distribution ( $C_x$ ), including the base pressure correction (Eq. 4), is approximately constant over the incidence range. The flow structures around the receiver change dramatically as incidence increases. For low angles of incidence between  $0 \leq \sigma_R \leq 6^\circ$ , the flow is generally attached but the crossflow component induces a thickening of the leeside boundary-layer. At higher incidence, the crossflow separates and rolls-up into two symmetric vortices (Hemsch 1992; Ericsson and Reding 1992). These dominate the leeside flow structure and pressure field and induce the non-linear vortex lift seen in Fig. 3.

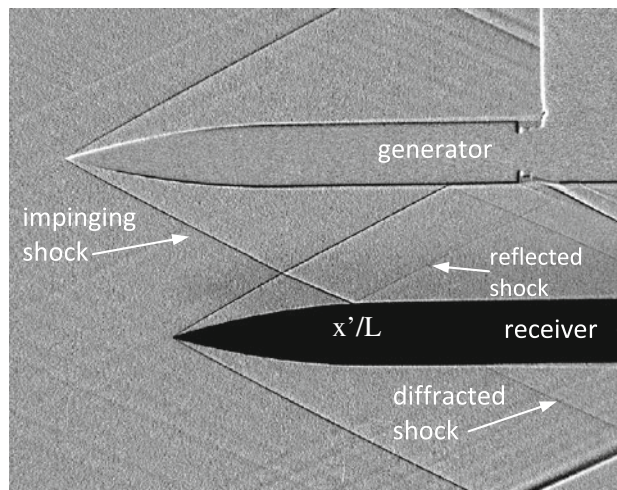


**Fig. 4** Measured shadowgraph visualisation:  $\Delta x/D = 1.67$   $\Delta z/D = 2.94$ ,  $\sigma_R = 0^\circ$ ,  $m2653$   $\sigma_G = 0^\circ$

### 3.2 Datum configuration

For the multi-body configurations, a datum case has been selected which consists of the receiver and sharp generator both at zero incidence ( $\sigma_R = 0^\circ$ ,  $\sigma_G = 0^\circ$ ) and an axial stagger of  $\Delta x/D = 1.67$ . The purpose of initially focusing on this datum configuration is to evaluate, in-depth, the different flow features associated with the interference aerodynamics and thereby facilitate the subsequent analyses for other configurations. The topology of the interference flowfield in this configuration is highlighted by the shadowgraph visualisation (Fig. 4). This shows that the generator bow shockwave impinges on the nearside ( $\phi = 180^\circ$ ) of the receiver body at  $x'/L = 0.4$ . A portion of the impinging shock then reflects back towards the generator body and the remainder diffracts to the farside ( $\phi = 0^\circ$ ). This is also illustrated in the receiver surface pressure distribution (Fig. 5) which primarily shows the nearside pressure rise and the subsequent diffracted shock path around the body.

Figure 6 shows a nearside pressure rise of approximately  $\Delta C_{p,\text{near}} = 0.09$  at  $x'/L = 0.4$ . Downstream of the axial impingement location, the local nearside pressure then reduces due to the expansion waves emanating from both receiver and generator forebodies (Figs. 5, 6). As the shock obliquely diffracts around the body, the local strength of the compression footprint initially attenuates. The shock diffracts on both sides of the receiver and eventually these separate diffracting shocks cross on the  $x-z$  plane of symmetry ( $\phi = 0^\circ$ ) at approximately  $x/L = 0.8$  (Fig. 5). This results in a further increase in the static pressure distribution where each diffracting shock is augmented by the perturbation that has crossed the symmetry plane. Consequently, towards the aft of the body there is a

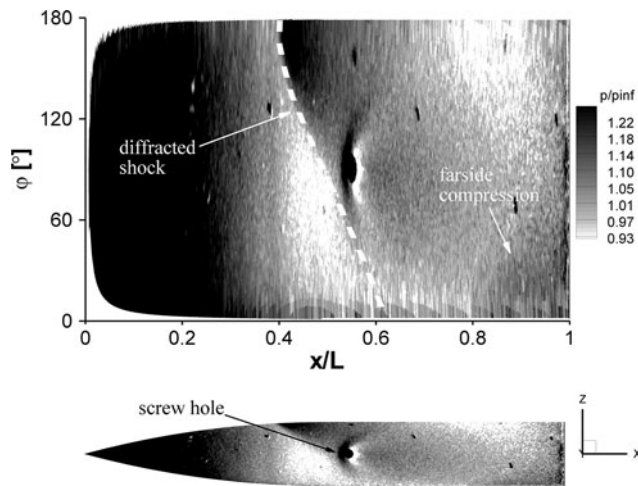


**Fig. 5** Measured receiver surface pressures highlighting the approximate shock path (dashed):  $\Delta x/D = 1.67$   $\Delta z/D = 2.94$ ,  $\sigma_R = 0^\circ$ ,  $m2653$   $\sigma_G = 0^\circ$

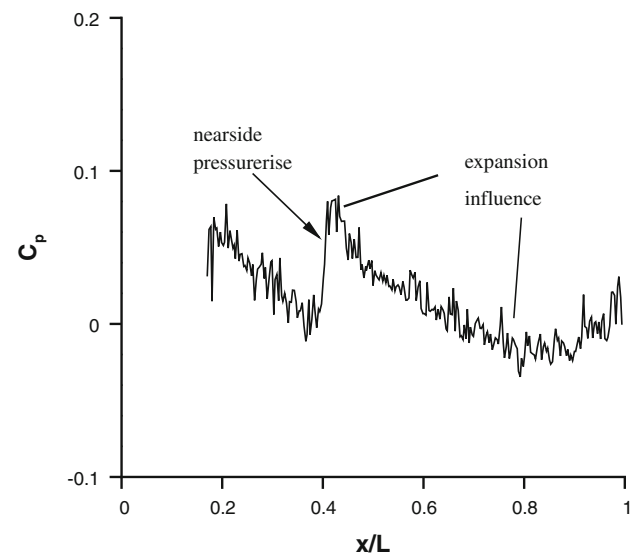


**Fig. 6** Receiver nearside ( $\phi = 177^\circ$ ) pressure distribution:  $\Delta x/D = 1.67$   $\Delta z/D = 2.94$ ,  $\sigma_R = 0^\circ$ ,  $m2653$   $\sigma_G = 0^\circ$

notable region of augmented pressure on the farside, which significantly affects the local and overall receiver aerodynamics (Fig. 5).

The interference loads ( $\Delta C_{X_i}$ ,  $\Delta C_Z$ ,  $\Delta C_m$ ) are defined as the change in force or moment from the isolated configuration. These interference loads (e.g.  $\Delta C_Z = C_Z - C_{Z,iso}$ ) primarily depend on the strength and location of the induced changes to the static pressure field on the body. As the interference has different complex local effects over the body, the overall changes depend on the relative impact of various elements. For example, in this datum case, the change in normal force primarily depends on the mix of the nearside expansion and farside compression footprints (increase in  $C_Z$ ) and the nearside compression footprint

(decrease in  $C_Z$ ). In this case, although the local changes are notable, these competing aspects are of approximately equal magnitude and result in a small overall  $\Delta C_Z = -0.02$ . However, due to the nearside expansion and farside compression footprints acting further aft on the receiver, there is a notable negative pitching moment interference load of  $\Delta C_m = -0.13$ . Finally, a negligible axial interference load is observed because of the limited area in the projected x-direction over which the interaction footprints act.

### 3.3 Effect of receiver incidence

As the receiver incidence increases from zero, there is a change in the underlying isolated aerodynamics, where the effects of flow separations, body vortices and the stream-wise load distribution become more significant. Furthermore, for the multi-body configurations, there is a change in the impinging shock strength and location. Consequently, as both the isolated receiver aerodynamics and the impact of the disturbance field are notably different, it is expected that the interference loads will also depend on the receiver incidence setting.

#### 3.3.1 Effect of receiver incidence on the force and moment characteristics

The receiver and sharp generator were arranged with an axial stagger of  $\Delta x/D = 1.67$  and  $\sigma_G = 0^\circ$ , while the receiver incidence was varied from  $\sigma_R = -15^\circ$  to  $\sigma_R = 15^\circ$ . The induced  $\Delta C_Z$  and  $\Delta C_m$  are found to vary non-monotonically with incidence and the effects are a minimum when the receiver is at approximately zero incidence (Fig. 7). The magnitude of the interference loads generally increase as the receiver is pitched either up or down. Moreover, the interference is typically larger at positive rather than negative incidence with maximum loads of  $\Delta C_Z = -0.18$  and  $\Delta C_m = 0.43$  induced at  $\sigma_R = 14^\circ$  and  $\sigma_R = 12^\circ$ , respectively. This equates to a change of effective incidence of  $\sigma_{eff} = -3.0^\circ$  based on  $\Delta C_Z$  and  $\sigma_{eff} = -2.2^\circ$  based on  $\Delta C_m$ . For this configuration, the longitudinal centre of pressure location moves aft from  $X_{cp}/D = 3.6$  to  $3.8$  between the isolated and multi-body cases (Fig. 8). Moreover, across the positive incidence range the interference effects always result in an aftward movement of  $X_{cp}$ . This stabilising change in  $X_{cp}$  significantly increases for lower positive incidence settings and can be as large as  $\Delta X_{cp}/D = 3$ . For the simple, unfinned model used as the receiver in these tests the reference  $X_{cg}/D = 4.44$  is included for comparison. A different characteristic is observed for the configurations with the receiver at negative incidence. At large negative incidence, there is no change in  $X_{cp}$  but in the range  $-1 \leq \sigma_R \leq 6^\circ$ ,

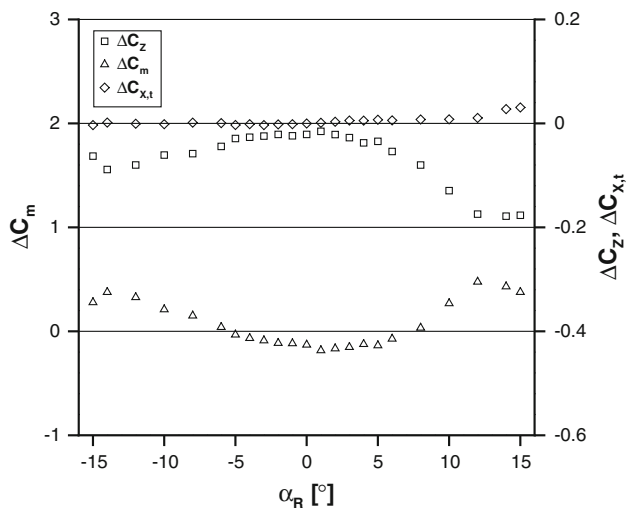


**Fig. 7** Effect of receiver incidence on interference loads:  $\Delta x/D = 1.67$   $\Delta z/D = 2.94$ ,  $m2653$   $\sigma_G = 0^\circ$

the centre of pressure moves forward by up to  $\Delta X_{cp}/D = 2$  (Fig. 8). Finally, the axial force interference is effectively zero except at high, positive incidence but the magnitudes are generally small with a maximum of  $\Delta C_{X,t} = 0.03$  (Fig. 7).

### 3.3.2 Effect of receiver incidence on the structure of the interference flowfield

The underlying aerodynamic mechanisms are examined using the PSP measurements which were obtained for the interference configurations with  $\sigma_R = 0, \pm 8, \pm 15^\circ$ . A change in receiver incidence affects a range of important parameters which characterise the interference aerodynamics. Some of these principal parameters are the axial impingement location ( $x'/L$ ), impinging shock strength, reflected shock strength, local expansion strength and the shock obliqueness angle ( $\theta_{obl}$ , Fig. 9b). As the receiver incidence increases over the range  $-15 \leq \sigma_R \leq 15^\circ$ , the axial impingement location moves forward from  $x'/L = 0.55$  to  $x'/L = 0.09$  (Fig. 9a–d). The shadowgraph visualisation (Fig. 9a) and the associated surface pressure contours (Fig. 10a) for the  $\sigma_R = 15^\circ$  configuration show that in this case the impinging shock does not diffract to the farside of the receiver body as a result of the shock angle and geometric arrangement. The shock structure for the other incidence settings is similar to the datum topology where the shock diffracts to the farside of the receiver (Fig. 10b–d). The shock obliqueness angle is defined as the difference between the generator conical shock angle and the receiver body axis ( $\theta_{obl} = \theta_{s,G} - \sigma_R$ ). This decreases from  $\theta_{obl} = 43^\circ$  to  $\theta_{obl} = 13^\circ$  as the receiver incidence increases from  $\sigma_R = -15^\circ$  to  $\sigma_R = 15^\circ$  (Fig. 10a–d).

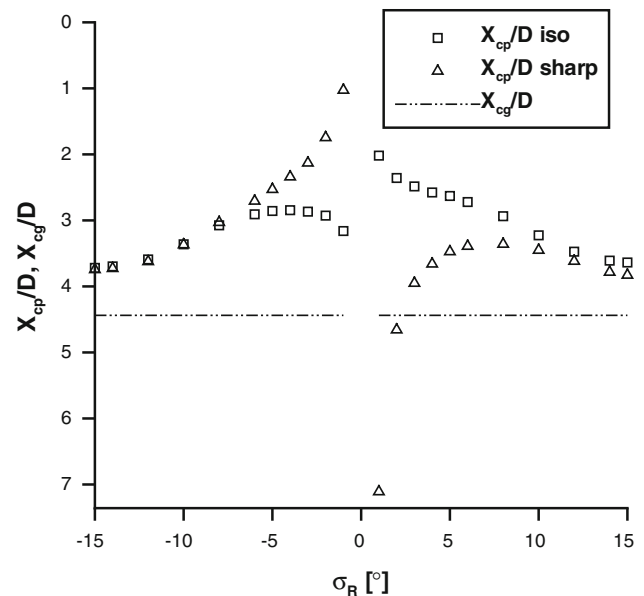


**Fig. 8** Effect of receiver incidence on  $X_{cp}$ :  $\Delta x/D = 1.67$   $\Delta z/D = 2.94$ ,  $m2653$   $\sigma_G = 0^\circ$

A decrease in  $\theta_{obl}$  decreases the extent of the farside interaction for a given  $x'/L$ . This reaches a minimum for  $\sigma_R = 15^\circ$  where the diffracted shock exits over the model base. The dashed lines in Fig. 10 highlight the approximate impinging shock paths. Although difficult to discern in the figures, these are determined from interrogation of the pressure contours, identifying where the shock footprint first raises the pressure above the isolated level.

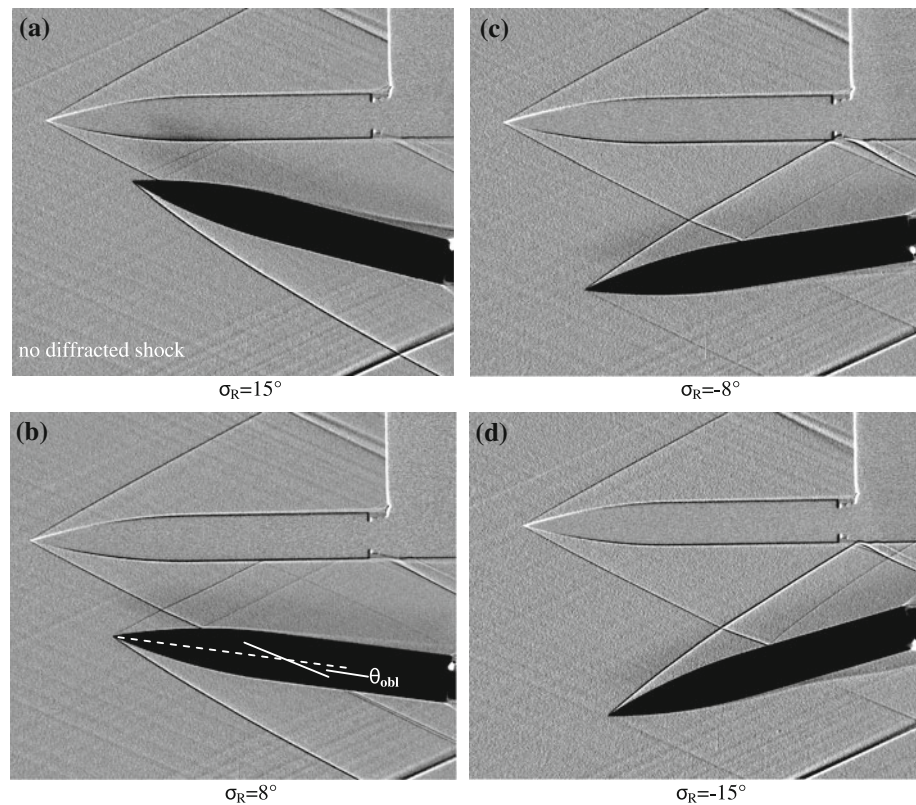
### 3.3.3 Effect of receiver incidence on the underlying flowfield mechanisms

Across the full receiver incidence range, the interference effects reduce the receiver normal force relative to the isolated body values (Fig. 7). In addition, the magnitude of  $\Delta C_Z$  is up to an order of magnitude larger when the body is placed at high incidence than in the datum configuration. It is known that the interference aerodynamic flow features comprise a range of elements, which individually either increase or decrease the changes to the local normal force distribution. These are discussed in this section for two configurations where the receiver is placed at  $\sigma_R = -15^\circ$  and  $\sigma_R = 15^\circ$  to help explain the effect of receiver incidence.

When the receiver is placed at  $\sigma_R = -15^\circ$ , two important changes from the datum interference configuration at  $\sigma_R = 0^\circ$  are noticed. First, the reflected shock strength increases due to the high flow turning necessary to maintain flow tangency with the downstream receiver surface. This results in a larger nearside pressure rise of  $\Delta C_{p,near} = 0.13$  (Fig. 11) and an augmented region of induced negative local normal force. Second, the strength of the expansion



**Fig. 9** Measured shadowgraph visualisations:  $\Delta x/D = 1.67$ ,  $\Delta z/D = 2.94$ , m2653  $\sigma_G = 0^\circ$  at **a**  $\sigma_R = 15^\circ$ , **b**  $\sigma_R = 8^\circ$ , **c**  $\sigma_R = -8^\circ$  and **d**  $\sigma_R = -15^\circ$



waves which impinge on the nearside are weaker as the receiver is further from the generator (Fig. 9d). There is therefore a reduction in the positive normal force elements for  $\sigma_R = -15^\circ$  compared to the datum configuration. In addition, the impact of the diffracted farside compression footprint is limited for this case because the surface pressure distribution is dominated by the body vortex flow. This also reduces the impact of the regions which experience a positive change in local normal force. All of these aspects reduce the interactions which induce regions of positive changes in local normal force in comparison with the datum configuration and augment the regions of negative changes in local normal force. Consequently, the interference loads are larger and  $\Delta C_Z$  is more negative than the datum configuration (Fig. 7).

When the receiver is placed at  $\sigma_R = 15^\circ$ , it is closer to the generator body than the datum case and the nearside pressure rise is dominated by the subsequent increase in the impinging shock strength ( $\Delta C_{p,\text{near}} = 0.12$ , Fig. 12). The axial impingement location ( $x'/L = 0.09$ ) in this configuration leads to a larger extent of the nearside compression footprint in comparison with the datum configuration ( $x'/L = 0.4$ ) and the negative normal force contribution is increased accordingly. In addition, at  $\sigma_R = 15^\circ$  the shock obliqueness angle ( $\theta_{\text{obl}}$ ) is such that the impinging shock does not diffract to the farside of the receiver body (Fig. 10a). This means there is no induced farside footprint

and the positive local normal force contribution is reduced compared to the datum case. These three observations explain why the magnitude of the normal force interference is greater at  $\sigma_R = 15^\circ$  relative to the datum configuration.

This  $\sigma_R = 15^\circ$  configuration also highlights why the magnitude of the interference loads are greater at positive than negative incidence. In general, the extent of the nearside compression footprint is larger when the body is at positive incidence. In addition, as the shock obliqueness angle increases for negative incidence angles, the extent of the farside compression increases accordingly. These characteristics increase the dominance of the interactions which induce regions of negative changes in local normal force for bodies at positive incidence. As a result, the normal force interference is three times larger at  $\sigma_R = 15^\circ$  than at  $\sigma_R = -15^\circ$  (Fig. 7).

The pitching moment interference effects are a function of the location and magnitude of the nearside and farside interactions. At low incidence ( $-6^\circ \leq \sigma_R \leq 6^\circ$ ), the effect of the nearside and farside interactions balance, which results in overall values of  $\Delta C_Z$  close to zero. However, as the interactions which induce regions of positive changes in local normal force occur further aft than the nearside compression there is a more negative pitching moment load ( $\Delta C_m$ ), Fig. 7. For  $\sigma_R \geq 6^\circ$ , the changes in normal force act near the receiver leading edge and induce large increases in the pitching moment interference load up to

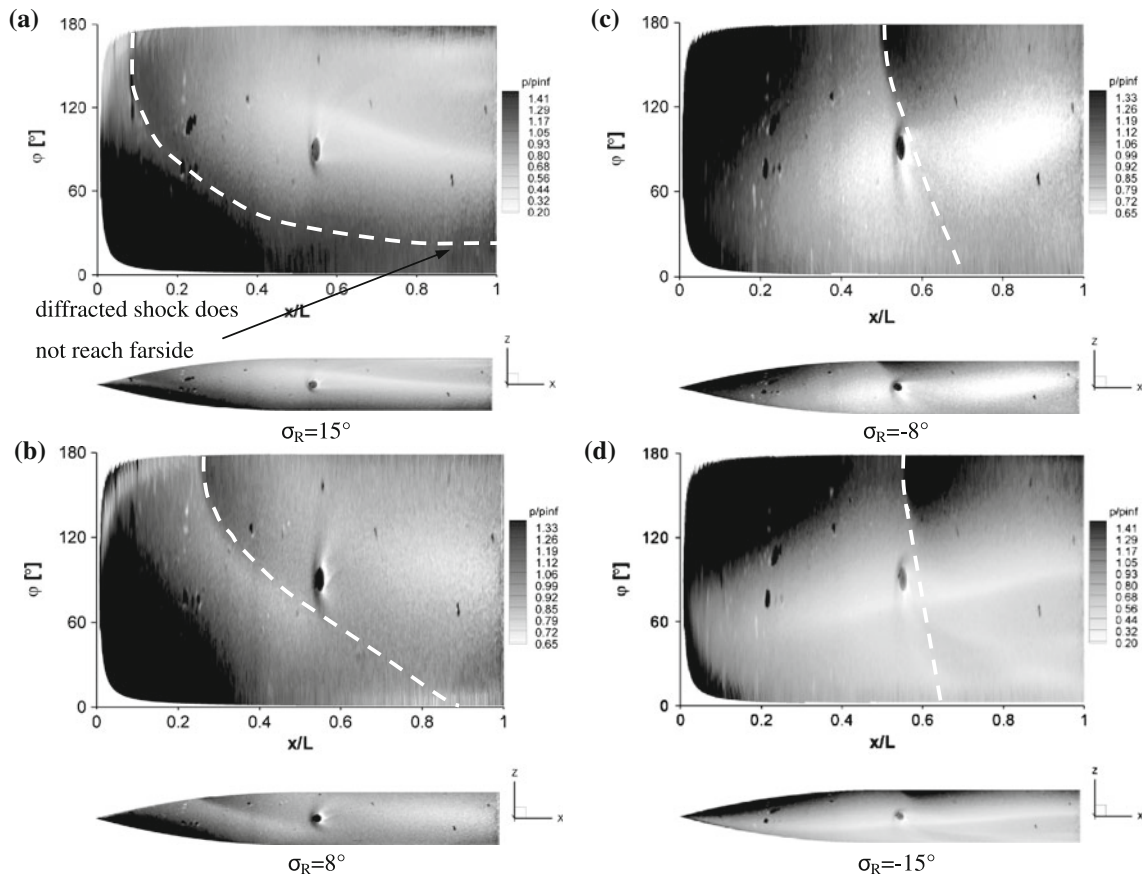


**Fig. 10** Measured receiver surface pressures highlighting approximate shock paths (*dashed*):  $\Delta x/D = 1.67$   $\Delta z/D = 2.94$ , m2653  $\sigma_G = 0^\circ$  at **a**  $\sigma_R = 15^\circ$ , **b**  $\sigma_R = 8^\circ$ , **c**  $\sigma_R = -8^\circ$  and **d**  $\sigma_R = -15^\circ$ . Note the different legend scales for clarity

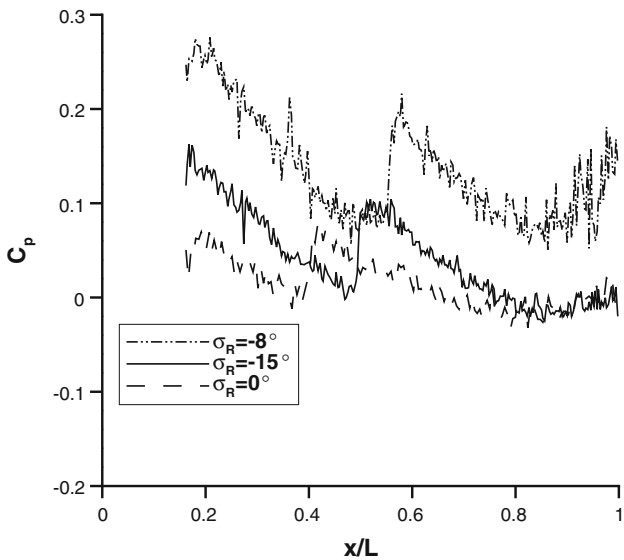


**Fig. 11** Receiver nearside pressure ( $\phi = 177^\circ$ ) distribution:  $\Delta x/D = 1.67$   $\Delta z/D = 2.94$ , m2653  $\sigma_G = 0^\circ$

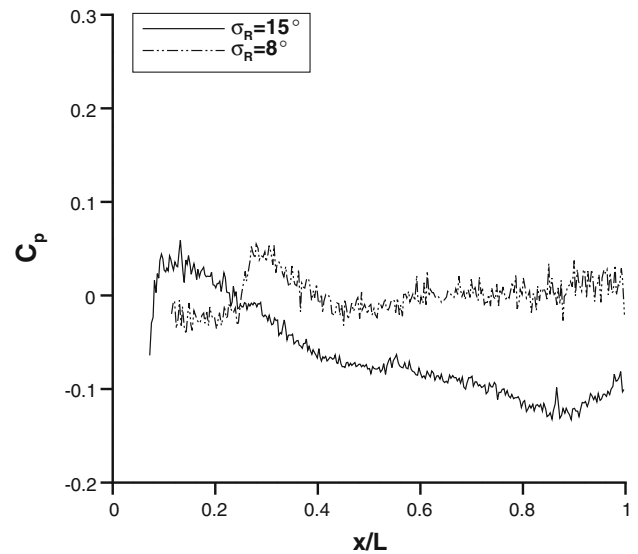


**Fig. 12** Receiver nearside pressure ( $\phi = 177^\circ$ ) distribution:  $\Delta x/D = 1.67$   $\Delta z/D = 2.94$ , m2653  $\sigma_G = 0^\circ$

$\Delta C_m = 0.48$  at  $\sigma_R = 12^\circ$  (Fig. 7). The nearside compression also dominates the pitching moment interference load for  $\sigma_R \leq -6^\circ$  and results in positive values of  $\Delta C_m$

(Fig. 7). However, these are generally smaller than the positive incidence cases because the impingement location ( $x'/L$ ) is further aft and the extent of the nearside

compression is less. Overall, there is not as marked a difference between the pitching moment at negative and positive incidence as there is for normal force due to the mitigating influence of changes in  $x'/L$  (Fig. 7).

Overall, the interference effects are up to an order of magnitude larger when the receiver is placed at incidence. The effect of receiver incidence is driven by the shock axial impingement location which determines the extent of the nearside interactions. Also important is the shock obliqueness angle, which affects the extent of the farside interaction, and the position of the receiver in the disturbance flowfield which affects the strength of all interaction footprints. The magnitudes of  $\Delta C_Z$  and  $\Delta C_m$  are largest when the shock does not diffract to the farside of the body.

### 3.4 Effect of a stronger disturbance flowfield

An increase in the strength of the disturbance flowfield was achieved using a blunt generator with a hemi-spherical forebody. At zero incidence, the pressure increase across the impinging shock ( $\Delta C_p$ ) increases by a factor of three compared to the sharp generator configuration. As well as changing the strength of the compression and expansion disturbances, the bow shock propagation angle is different. The axial impingement point is kept constant relative to the sharp generator case ( $x'/L = 0.4$  at  $\sigma_R = 0^\circ$ ) by changing the axial stagger from  $\Delta x/D = 1.67$  to  $\Delta x/D = -0.53$ . As with the sharp generator, the effect of incidence is examined over the range  $-15 \leq \sigma_R \leq 15^\circ$ .

#### 3.4.1 Effect of a stronger disturbance flowfield on the force and moment characteristics

Relative to the sharp generator configurations, the effect of the stronger disturbance field depends on the receiver incidence angle. For some arrangements, the blunt generator produces significant changes in both  $\Delta C_Z$  and  $\Delta C_m$  relative to the sharp generator configuration. At positive incidence ( $\sigma_R > 0^\circ$ ), there are relatively minor changes in  $\Delta C_Z$ , while at negative incidence ( $\sigma_R < 0^\circ$ ) the interference loads are almost doubled in some cases (e.g.  $\sigma_R = -12^\circ$ , Fig. 13). In addition, as with the sharp generator cases, the interference loads increase as the receiver body is placed at either positive or negative incidence in comparison with the zero incidence case. The changes in  $\Delta C_m$  due to the effect of the blunt generator can be notable but also depend on the receiver incidence. For example, at positive incidence,  $\Delta C_m$  is approximately tripled at  $\sigma_R = 5^\circ$  and at a negative incidence of  $\sigma_R = -14^\circ$  the  $\Delta C_m$  is almost doubled from 0.38 to 0.66 (Fig. 14). With the blunt generator, the pitching moment changes are not symmetric about  $\sigma_R = 0^\circ$  as the local

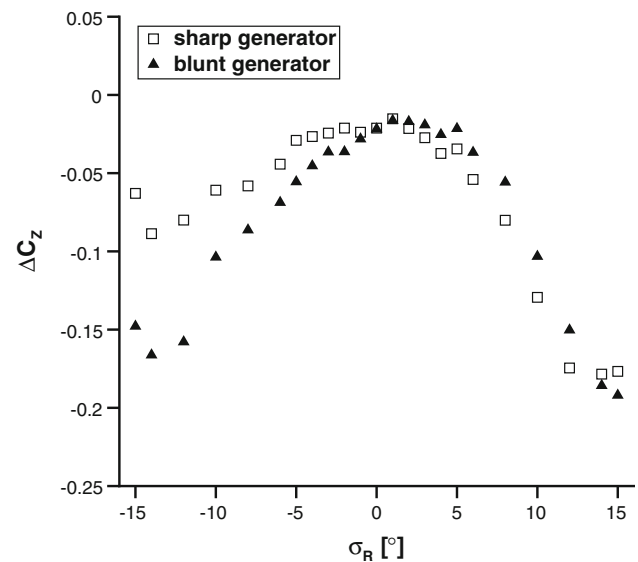


Fig. 13 Effect of blunt generator on normal force interference load

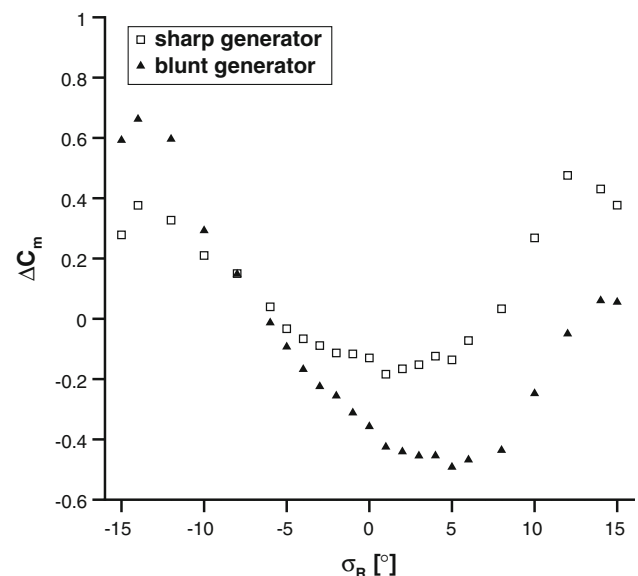
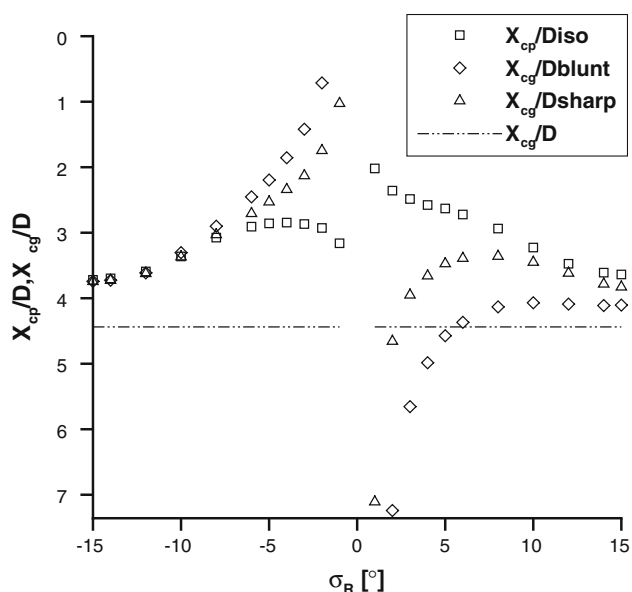


Fig. 14 Effect of blunt generator on pitching moment interference load

minimum  $\Delta C_m$  now occurs at  $\sigma_R = 5^\circ$ . Similar characteristics in the movements of  $X_{cp}$  are observed here as in the sharp generator configurations (Fig. 15). However, the movement of  $X_{cp}$  is amplified by up to a factor two. For the blunt generator configurations between  $1 \leq \sigma_R \leq 5^\circ$ , the interference flowfield moves the centre of pressure further aftward than the sharp case and so much so, that the body is statically stable over this range. Finally, the axial force interference load follows a similar trend to that observed for the sharp generator but reaches a larger maximum of  $\Delta C_{X,t} = 0.06$  at  $\sigma_R = 15^\circ$ .



**Fig. 15** Effect of receiver incidence on  $X_{cp}$ :  $\Delta x/D = -0.53$   $\Delta z/D = 2.94$ ,  $m2654$   $\sigma_G = 0^\circ$

### 3.4.2 Effect of a stronger disturbance flowfield on the structure of the interference flowfield

Using the blunt generator increases the impinging shock strength ( $\Delta C_p$  across the shock) compared to the sharp case at  $\sigma_R = 0^\circ$  by a factor of approximately three. As the generator is different there are also changes to  $\theta_{s,G}$  and  $x'/L$ . However, these are small, the shock angle for the approximately conical portion of the blunt generator bow shock is  $\theta_{s,G} = 28.6^\circ$ , which is similar to that for the sharp generator ( $\theta_{s,G} = 28.2^\circ$ ). Consequently, over the incidence range tested there is a negligible difference in axial impingement location between the sharp and blunt cases for most configurations. The largest difference in impingement location between the sharp and blunt cases is  $x'/L = 0.07$  which occurs at  $\sigma_R = 15^\circ$ . As well as changing the shock strength, the blunt generator also has a different expansion wave field, which affects the interference aerodynamics. The hemispherical forebody induces stronger expansion waves, which act over a smaller extent compared to the sharp generator case.

The principal features of the interference flowfield for the blunt generator configurations are similar to those with the sharp generator (Fig. 16a–e). A notable exception is for  $\sigma_R = 15^\circ$ , where the impinging shock diffracts to the far-side of the receiver body (Fig. 16a) whereas for the sharp generator case it does not (Fig. 9a). In this configuration, a double-shock structure on either side of the separated flow region propagates around the receiver body. Similarly, the interaction footprints highlighted by the receiver surface pressures (Fig. 17a–e) show comparable flow structures to

the sharp generator cases, except for  $\sigma_R = 15^\circ$  and  $\sigma_R = 8^\circ$ . In these cases, there is evidence of a local shock-induced separation of the boundary-layer. The low-pressure plateau (Fig. 17a, b) along with the double-reflected shock structure (Fig. 16a, b) either side of the separation region were also observed by Brosh et al. 1985. The additional vortex flow feature is expected to be a horseshoe vortex (Fig. 16a) and the double diffracted shock structure in the  $\sigma_R = 15^\circ$  case also supports this interpretation.

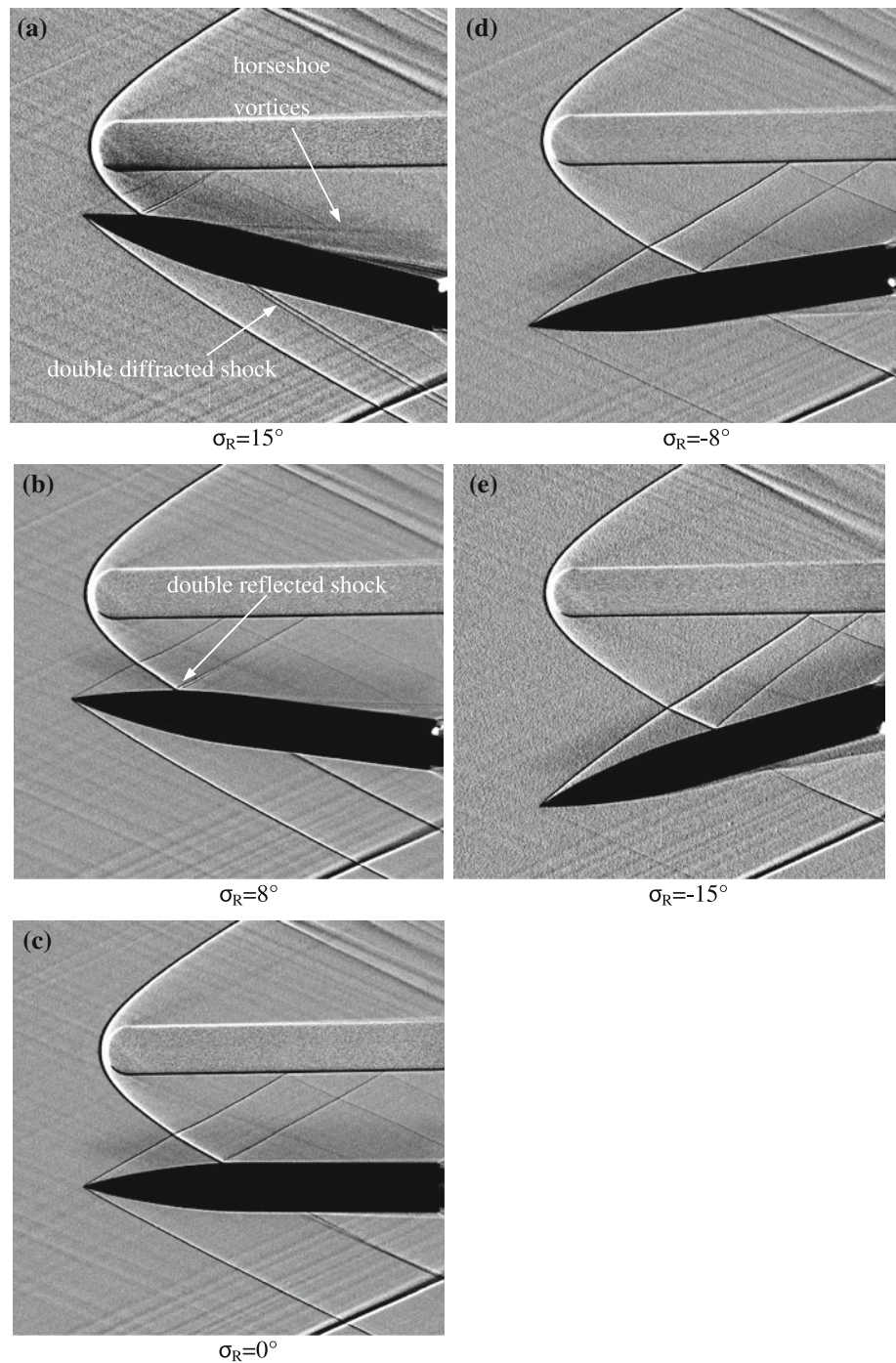
### 3.4.3 Effect of a stronger disturbance flowfield on the underlying flowfield mechanisms

The effect of the blunt generator on the underlying flowfield mechanisms is investigated for three configurations ( $\sigma_R = -15, 0, 15^\circ$ ), where the observed characteristics are different. A key finding is that the  $\Delta C_Z$  more than doubles for  $\sigma_R = -15^\circ$  compared to the sharp generator configuration, whereas there is no difference for  $\sigma_R = 0^\circ$  and  $\sigma_R = 15^\circ$ . In this section, the presented surface pressure comparisons between the blunt and sharp generator configurations have been corrected to overlie upstream of the impingement location.

At  $\sigma_R = 0^\circ$ , relative to the sharp generator configuration, the blunt generator produces a negligible overall change in  $\Delta C_Z$  and an increase in the magnitude of  $\Delta C_m$  (Fig. 14). As expected, the stronger impinging shock (Fig. 18) induces a more significant region of negative local normal force. However, because the receiver is close to the generator body the interactions which induce regions of positive changes in local normal force are also significant. The nearside impinging expansion waves (Fig. 18) along with the farside compression footprint induce an augmented region of positive local normal force (Fig. 19). This balances the effect of the stronger nearside compression footprint and there is no overall change in normal force in comparison with the sharp generator case. In this configuration, the pitching moment is dominated by the region of positive local normal force acting near the trailing edge of the receiver and this increases the magnitude of  $\Delta C_m$  from  $\Delta C_m = -0.13$  to  $\Delta C_m = -0.36$  compared to the sharp generator case (Fig. 14).

For the  $\sigma_R = -15^\circ$  configuration, the shock impinges at the same location as the sharp generator ( $x'/L = 0.54$ ), but the initial nearside pressure rise is larger by a factor of 2.5 ( $\Delta C_{p,near} = 0.3$ ), Fig. 20. Consequently, this acts to increase the magnitude of the normal force interference. The local pressure then reduces at a greater rate than the sharp case, due to the influence of the stronger expansion field induced by the hemi-spherical forebody. The shock diffracts to the receiver farside and induces a farside compression footprint (Fig. 21). However, it is thought that the diffracted shock interacts with the body vortex on the

**Fig. 16** Measured shadowgraph visualisations:  $\Delta x/D = -0.53$   $\Delta z/D = 2.94$ ,  $m2654$   $\sigma_G = 0^\circ$  at **a**  $\sigma_R = 15^\circ$ , **b**  $\sigma_R = 8^\circ$ , **c**  $\sigma_R = 0^\circ$ , **d**  $\sigma_R = -8^\circ$  and **e**  $\sigma_R = -15^\circ$



leeside (farside) and the local pressure rise is less that would otherwise have been expected. This interpretation is supported by Computational Fluid Dynamics (CFD) studies (Chaplin 2009). Overall, the blunt generator increases the magnitude of the regions of the receiver which experience both positive and negative changes in local normal force. However, the more significant nearside compression leads to an increase in the interaction affect, where  $\Delta C_Z$  increases in magnitude from  $\Delta C_Z = -0.06$  to  $\Delta C_Z = -0.15$  in

comparison with the sharp generator configuration (Fig. 13). The dominance of the nearside compression footprint concurrently leads to an increase in the magnitude of the overall pitching moment by  $\Delta C_m = 0.3$  compared to the sharp case (Fig. 14).

Different aerodynamic characteristics are observed when the receiver incidence is  $\sigma_R = 15^\circ$ . In this configuration, the impinging shock diffracts to the farside and leads to a compression of the local pressure distribution

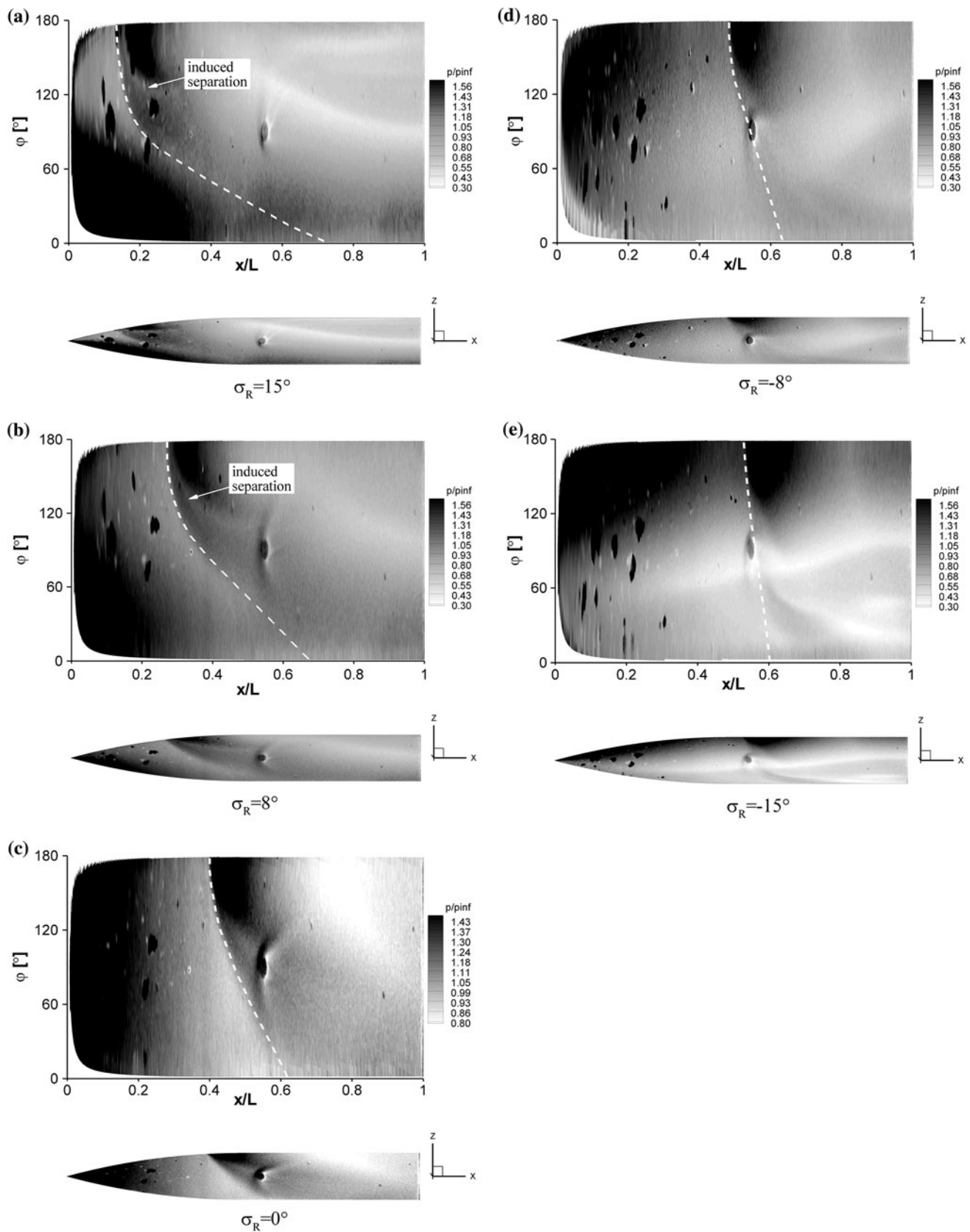


**Fig. 17** Measured receiver surface pressures highlighting approximate shock paths (*dashed*):  $\Delta x/D = -0.53$   $\Delta z/D = 2.94$ , m2654  $\sigma_G = 0^\circ$  at **a**  $\sigma_R = 15^\circ$ , **b**  $\sigma_R = 8^\circ$ , **c**  $\sigma_R = 0^\circ$ , **d**  $\sigma_R = -8^\circ$  and **e**  $\sigma_R = -15^\circ$ . Note the different legend scales for clarity

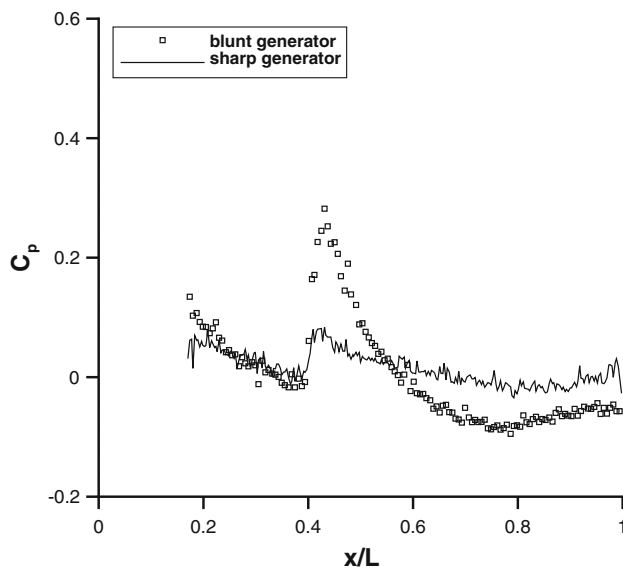


**Fig. 18** Effect of blunt generator on receiver nearside ( $\phi = 177^\circ$ ) PSP pressure distribution:  $\sigma_R = 0^\circ$

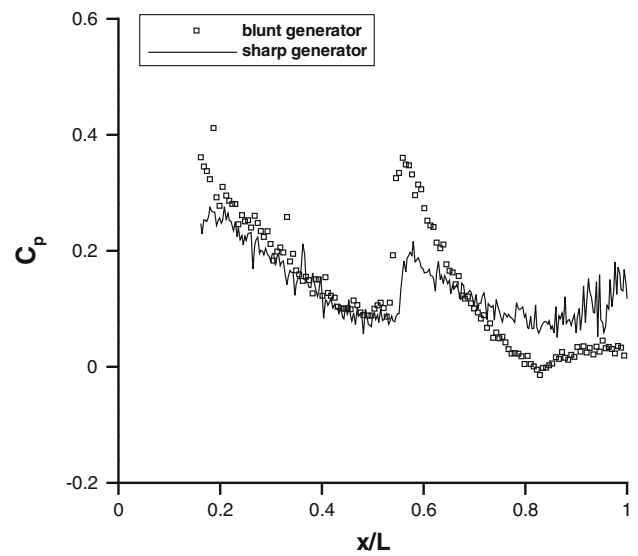


**Fig. 20** Effect of blunt generator on receiver nearside ( $\phi = 177^\circ$ ) PSP pressure distribution:  $\sigma_R = -15^\circ$

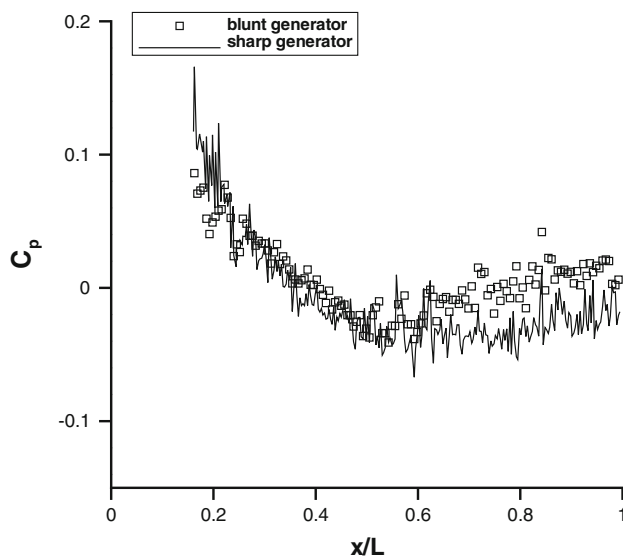


**Fig. 19** Effect of blunt generator on receiver farside ( $\phi = 3^\circ$ ) PSP pressure distribution:  $\sigma_R = 0^\circ$

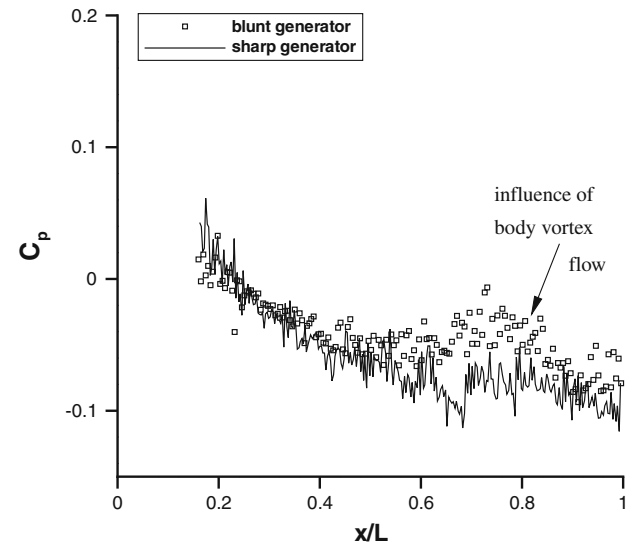


**Fig. 21** Effect of blunt generator on receiver farside ( $\phi = 3^\circ$ ) PSP pressure distribution:  $\sigma_R = -15^\circ$

(Fig. 17a). The increase in the magnitude of the nearside compression, relative to the sharp generator case, is offset by the increase in the strength of the local impinging expansion waves and the presence of the farside compression. As a result, these competing aspects balance and there is little difference to the normal force between the sharp and blunt generator cases.

In general, the blunt generator increases the magnitude of the normal force interference compared to the sharp cases. However, due to the impact of stronger expansion waves from the generator forebody and the intricacies

relating to shock diffraction, there are some configurations where there is only a small effect on the normal force.

The effect of the blunt generator on pitching moment is more case specific than the normal force characteristics. Even when there is no significant change in  $\Delta C_Z$  ( $\sigma_R \geq 0^\circ$ ), the interference has a larger effect on the pitching moment (Fig. 14). Two informative configurations for the effect of the blunt generator on  $\Delta C_m$  are the  $\sigma_R = 8^\circ$  and  $\sigma_R = -8^\circ$  configurations, where there is no change in  $\Delta C_m$  for  $\sigma_R = -8^\circ$  and an increase in the magnitude of  $\Delta C_m$  by 0.6 for  $\sigma_R = 8^\circ$ . For  $\sigma_R = 8^\circ$ , the impinging expansion waves are stronger for the blunt generator and thus the magnitude

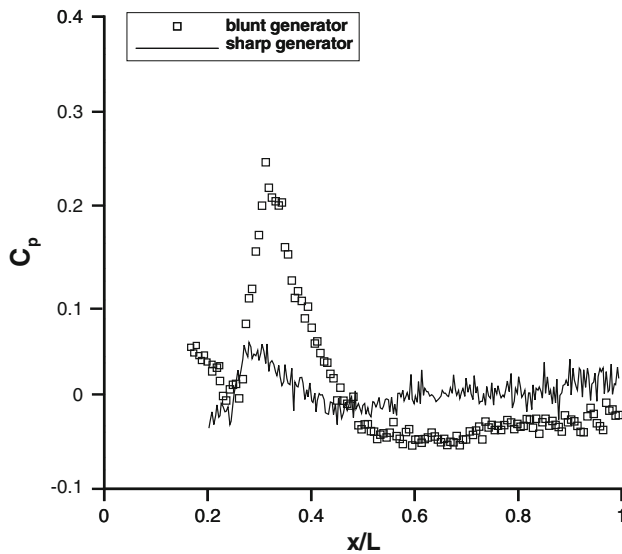


**Fig. 22** Effect of blunt generator on receiver nearside ( $\phi = 177^\circ$ ) pressure distribution:  $\sigma_R = 8^\circ$

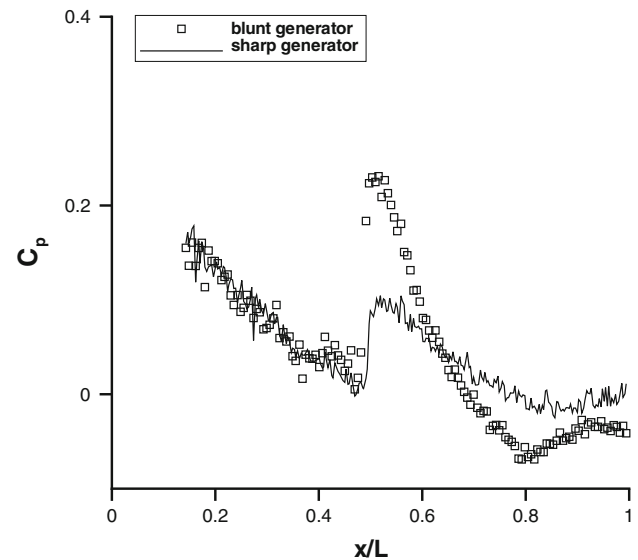


**Fig. 24** Effect of blunt generator on receiver nearside ( $\phi = 177^\circ$ ) pressure distribution:  $\sigma_R = -8^\circ$

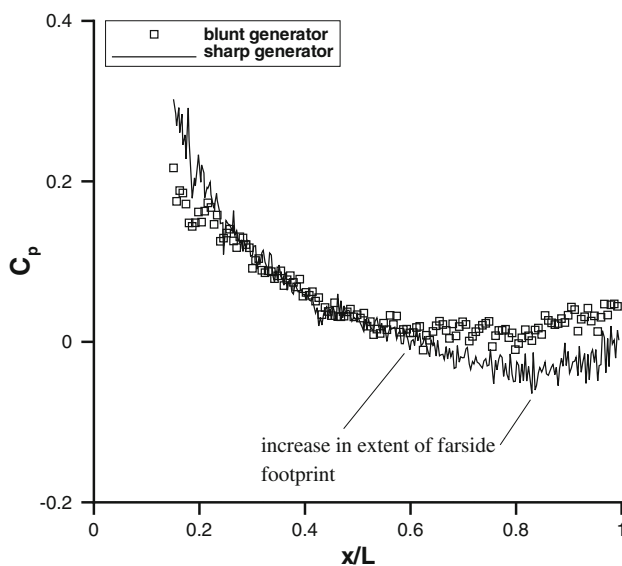


**Fig. 23** Effect of blunt generator on receiver farside ( $\phi = 3^\circ$ ) pressure distribution:  $\sigma_R = 8^\circ$

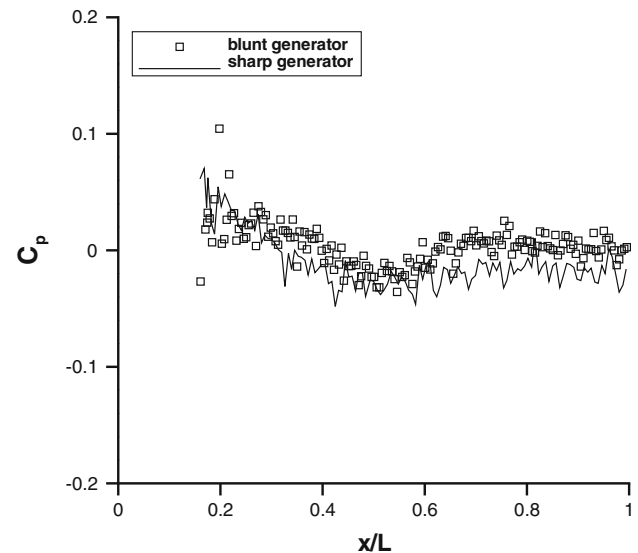


**Fig. 25** Effect of blunt generator on receiver farside ( $\phi = 3^\circ$ ) pressure distribution:  $\sigma_R = -8^\circ$

of the pressure gradient following the initial rise is greater than the sharp case (Fig. 22). Moreover, it is postulated that the shock diffracts to the farside further fore than the sharp case (Fig. 23) as a result of the viscous shock-interaction with the boundary-layer (Chaplin 2009). Both of the above points highlight the increased dominance of the region of positive local normal force between the blunt and sharp generator. This leads to a more negative  $\Delta C_m$  (Fig. 14).

For  $\sigma_R = -8^\circ$ , the nearside compression footprint is augmented as a result of the increased impinging shock strength, as previously described (Fig. 24). Similarly, the

magnitude of the nearside expansion increases due to the blunt generator and there is a very limited augmentation in the farside compression footprint (Fig. 25). As a result of the aftward impingement location, the region of positive local normal force is far from the moment reference point and contributes a significant amount to the overall  $\Delta C_m$ . Consequently, this balances the increases in  $C_m$  induced by the nearside compression footprint and there is no overall change in  $\Delta C_m$ . This shows that even sizable changes in normal force are not necessarily accompanied by a change in pitching moment and that the impingement location has a significant effect on  $\Delta C_m$ .



## 4 Conclusions

The aerodynamic interference between two slender bodies is investigated through a series of wind tunnel experiments utilising pressure sensitive paint, force and moment measurements and shadowgraph visualisations.

The PSP measurements are a useful tool in the analysis of multi-body interference due to the complex and distributed nature of the interaction pressure footprints. The multi-body flowfield is highly complex, particularly when the receiver body is at incidence. It includes impinging shock and expansion waves, shock diffraction and strong interaction of the impinging shock with the boundary-layer and body vortex flows. The impact of the diffracted shock on the local and overall aerodynamics is significant. The overall interference loads are a function of the relative strength, and location of the nearside and farside interactions.

The aerodynamic characteristics tend to be bespoke to each configuration, and it is difficult to extract overall trends. However, in general, the interference loads are largest when the receiver is at incidence although the peak effects on normal force and pitching moment are not coincident. The interference loads are strongly sensitive to the axial impingement location of the impinging shock and this is the dominating factor which determines the magnitude of the interference effects for a given disturbance field. When the strength of the disturbance field is increased the resulting changes in the interference loads strongly depend on the receiver incidence. For some incidence settings, the stronger disturbance field has almost no effect. However, at other settings the stronger disturbance flowfield amplifies the interference effects by a factor of two.

Maximum interference loads of up to  $\Delta C_Z = -0.19$  and  $\Delta C_m = 0.66$  were measured at a receiver incidence of  $\sigma_R = 15^\circ$  and  $\sigma_R = -14^\circ$ , respectively. This is an effective incidence of  $\sigma_{\text{eff}} = -3.2^\circ$  based on  $\Delta C_Z$  and  $\sigma_{\text{eff}} = -3.6^\circ$  based on  $\Delta C_m$ . At positive incidence, the interference tends to stabilise the body with a resulting aftward movement in longitudinal centre of pressure of up to two calibres for the configurations using the sharp generator. An opposite destabilising effect is observed when the receiver is at small negative incidence angles. These effects are also amplified when the disturbance strength is increased.

Overall, the results from this study provide an in-depth understanding for different steady-state multi-body configurations. In a dynamic store release situation, it is expected that for configurations where the interference loads are comparable to the isolated body loads (as at low incidence) there will be a notable change in the subsequent

body trajectories. In a situation where a pitch-up moment is induced on the receiver body, this may lead to a collision between the bodies.

**Acknowledgments** The authors would like to thank the UK MOD Defence Science and Technology Laboratory for both funding and providing technical support for this research. The first author was also partially funded through an Industrial CASE award from the UK Engineering and Physical Sciences Research Council.

## References

- Brosh A, Kussoy M, Hung C (1985) Experimental and numerical investigation of a shock wave impingement on a cylinder. *AIAA J* 23(6):840–846
- Chaplin R (2009) Aerodynamic interference between high-speed slender bodies. PhD Dissertation, Cranfield University, UK
- Derunov E, Zheltovodov A, Maksimov A (2008) Development of three-dimensional turbulent separation in the neighborhood of incident crossing shock waves. *Th&Ae* 15(1):29–54
- Ericsson L, Reding J (1992) Asymmetric flow separation and vortex shedding of bodies of revolution. In: Hemsch M (ed) *Tactical missile aerodynamics: general topics*. American Institute of Aeronautics and Astronautics, Washington, pp 391–452
- Fedorov A, Malmuth N, Soudakov V (2007) Supersonic scattering of a wing-induced incident shock by a slender body of revolution. *J Fluid Mech* 585:305–322
- Gregory J, Asai K, Kameda M, Lui T, Sullivan J (2008) A review of pressure-sensitive paint for high-speed and unsteady aerodynamics. *Proc Inst Mech Eng G J Aerosp Eng* 222:249–290
- Hemsch M (1992) *Tactical missile aerodynamics: general topics*. American Institute of Aeronautics and Astronautics, Washington
- Hung C (1985) Computation of three-dimensional shock wave and boundary-layer interactions. NASA Technical Memorandum 86780
- Kurita M, Okada T, Nakamura Y (2001) The effects of attack angle on side jet aerodynamic interaction in a blunted body at hypersonic flow. *AIAA Paper* 2001-1825
- Lui T, Sullivan J (2005) *Pressure and temperature sensitive paints*. Springer-Verlag, Berlin
- Malmuth N, Shaleav V (2004) theoretical modelling of interaction of multiple slender bodies in supersonic flows. *AIAA Paper* 2004-1127
- Morkovin M, Migotsky E, Bailey H, Phinney R (1952) Experiments on interaction of shock waves and cylindrical bodies at supersonic speeds. *J Aerosp Sci* 19(4):237–247
- Pulkin E, Carlson B, Gouin S, Costin C, Green E, Ponomarev S, Tanji H, Gouterman M (2000) Ideality of pressure-sensitive paint. 1. platinum tetra(pentafluorophenyl)porphine in fluoroacrylic polymer. *J Appl Polym Sci* 77:2795–2804
- Taylor J (1997) *An introduction to error analysis*. University Science Books, California
- Volkov V, Derunov E (2006) Interaction of a combination of bodies in supersonic flow. interference and diffraction of shock waves in flow over two bodies of revolution. *J Eng Phys Thermophys* 79(4):712–721
- Wilcox F (1995) separation characteristics of generic stores from lee side of an inclined flat plate at Mach 6. NASA Technical Memorandum 4652